


Article

Chemical and Temperature Sensors Based on Functionalized Reduced Graphene Oxide

Esteban Araya-Hermosilla ¹, Matteo Minichino ², Virgilio Mattoli ¹ and Andrea Pucci ^{2,3,*}

¹ Center for Micro-BioRobotics @SSSA Istituto Italiano di Tecnologia Viale Rinaldo Piaggio 34, 56025 Pontedera, Italy; esteban.araya@iit.it (E.A.-H.); virgilio.mattoli@iit.it (V.M.)

² Department of Chemistry and Industrial Chemistry, University of Pisa, Via Moruzzi 13, 56124 Pisa, Italy; minichino.matteo@gmail.com

³ CISUP, Centro per l'Integrazione della Strumentazione dell'Università di Pisa, Lungarno Pacinotti 43, 56126 Pisa, Italy

* Correspondence: andrea.pucci@unipi.it; Tel.: +39-050-221-9270

Received: 30 May 2020; Accepted: 19 June 2020; Published: 21 June 2020



Abstract: In this work, we investigated the functionalization of reduced graphene oxide (rGO) with 2-(dodecen-1-yl) succinic anhydride (TPSA) to increase the rGO effective interactions with organic solvents both in liquid and vapor phases. Thermogravimetric analysis, STEM, XPS, FTIR-ATR, and Raman spectroscopy confirmed the effective functionalization of rGO with about the 30 wt % of grafted TPSA without affecting the structural characteristics of graphene but successfully enhancing its dispersibility in the selected solvent except for the apolar hexane. Solid TPSA-rGO dispersions displayed a reproducible semiconducting (activated) electrical transport with decreased resistance when heated from 20 °C to 60 °C and with a negative temperature coefficient of 10^{-3} K^{-1} , i.e., comparable in absolute value with temperature coefficient in metals. It is worth noting that the same solid dispersions showed electrical resistance variation upon exposure to vapors with a detection limit in the order of 10 ppm and sensitivity α of about 10^{-4} ppm^{-1} .

Keywords: graphene; reduced graphene oxide; covalent functionalization; chemical and temperature sensor

1. Introduction

Graphene is a two-dimensional crystal made of carbon atoms united by sp^2 sigma bonds [1–3]. The rest of the sp^2 orbitals that do not contribute to the crystal frame create the π -bonds network responsible for its outstanding electrical properties [4]. Graphene displays other excellent features such as high thermal conductivity [5], mechanical strength [6], negative thermal expansion [7], and optical transparency [8]. Due to these properties, graphene has found applications in diverse areas such as supercapacitors [9,10], antibacterial scaffolds [11], photovoltaic cells [12], biosensing [13], and transparent electronics [14]. In addition, its conductivity increases upon increasing the temperature, which has been exploited along with its high flexibility to build temperature sensors [15]. Chemosensors use graphene as active layer for sensing toxic gases and vapors [16]. These materials rely on the change of the electrical resistance in response to the adsorption of vapor analytes [16–19] such as NO_2 [20], NH_3 [21], CO [22], and volatile organic compounds (VOCs) [23] with high sensibility, selectivity, and reversibility [24,25]. The success of graphene as a chemosensor is not surprising since it has characteristic impermeability to gases [26], large specific surface area ($2630 \text{ m}^2/\text{g}$) [27], combined with excellent electrical conductivity [28], and low electrical noise [29].

Due to the high demand for graphene, scientists have developed diverse methods for its production and based on the two general bottom-up and top-down approaches [30]. The first involves the chemical vapor deposition [31,32], the growth from metal-carbon melt [33], and the epitaxial growth [34]. The second comprises micromechanical exfoliation (the scotch tape) [35], graphite exfoliation [36], and the ball milling method [37]. Although the techniques mentioned above may produce high-quality graphene, they are cumbersome, expensive, or the production results in low yields [30]. Graphite oxide (GO) has called close attention as a precursor of graphene because it is easy to produce in high quantities from graphite and yields stable dispersion in various solvents [38,39]. This method uses strong acids and oxidants to modify graphite [40–42] and yields to the formation of hydroxyl, carboxylic acid, and epoxy groups over the graphitic layer [43]. The incorporation of these groups makes graphite hydrophilic [44], thus facilitating its exfoliation as individual sheets in water and in polar organic solvents [45,46]. Unfortunately, the oxidation disrupts the conjugation of the hexagonal graphene lattice considerably, thus making GO an insulator [47,48]. However, GO can effectively recover its electric properties to some extent when reduced graphene oxide (rGO) is produced by chemical or thermal reduction treatments [49–51]. It is also found that the residual functional groups in the rGO structure favors the graphene dispersion in aqueous and polar media thanks to the effective interactions between the two materials [52–55].

Noteworthy, residual oxygen-functional groups of rGO provide reactive sites for further covalent functionalization aimed at extending rGO dispersibility in different class of solvents [56], thus favoring the formation of graphene layers by using simple and low-cost solution techniques such as drop casting [57], vacuum filtration [58], dip coating [59], and spin coating [60]. Additionally, thanks to the extra functionalities, rGO show excellent affinity to different vapor analytes in comparison to graphene [16] such as alcohols [61], Cl₂ [62], NO₂ [19,63], and ketones [64].

In connection with these findings, in this work, we report the easy functionalization of rGO with 2(dodecen-1-yl) succinic anhydride (TPSA) with the aim to increase the affinity of the graphitic core with some of the most common volatile solvents, and to provide solid dispersions with enhanced resistive sensing features (Figure 1). TPSA and in general alkenyl succinic anhydrides (ASA), are modified five-membered succinic anhydrides bearing a linear or branched iso-alkenyl chain. These molecules are colorless viscous liquids that are widely employed in the paper industry for the hydrophobization of cellulose fibers or as building blocks for detergents in fuels [65,66]. The final TPSA-rGO product was characterized via thermogravimetric analysis (TGA), Raman spectroscopy, ATR-FTIR, XPS, and scanning transmission electron microscopy (STEM) to determine the amount of TPSA grafted on the graphitic core as well as its structural characteristics. TPSA-rGO was studied in terms of its dispersibility into five different organic solvents and the sensing characteristics of the derived solid films eventually evaluated as a function of temperature changes and the exposure to vapors of volatile solvents.

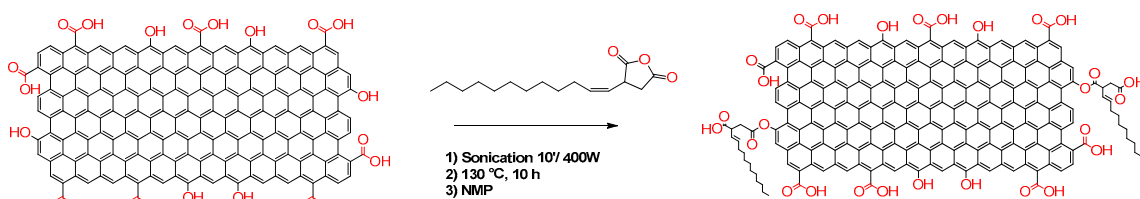


Figure 1. Functionalization of rGO with 2-(dodecen-1-yl) succinic anhydride (TPSA).

2. Experimental

2.1. Materials

Reduced graphene oxide (rGO) was purchased from Sigma-Aldrich, Italy, and used without any purification. It is composed of >75% C and <5% N, has a surface area of 103 (m²/g) and an electric conductivity of 7111 S/m (as reported by the manufacturer). Chloroform (99.5%), 1-methyl-2-pyrrolidone (99.5%), hexane (>95%), tetrahydrofuran (99.7%), and toluene (99.8%) were used as received (Sigma-Aldrich, Italy).

2.2. rGO Chemical Functionalization

50 mg of TPSA and 15 mg of rGO were dissolved in 50 mL of 1-methyl-2-pyrrolidone in a 100 mL beaker. The mixture was sonicated for 10 min at 400 W and 24 kHz with UP 400 S probe in titanium with a 3 mm diameter tip and 100 mm length (Hielscher's H3). During sonication, the beaker was immersed in an ice bath to prevent excessive temperature rise. Then, the dispersion was transferred in a 100 mL flask equipped with a condenser and a stirring bar. The reaction was stirred for 10 h at 130 °C. After cooling, the TPSA-rGO was precipitated in 1L of deionized water and recovered by filtration using a sartorius filter (Durapore®) with a PVDF filter membrane with a pore size of 0.22 µm and a diameter of 47 mm. The product was washed with deionized water, acetone, and ethyl ether to remove the solvent and the excess of unreacted TPSA. The functionalized graphene (TPSA-rGO) was then dried under vacuum for 24 h.

2.3. Preparation of the rGO Dispersions and Setup Preparation for the Resistive Measurements

5 mg of rGO or TPSA-rGO were poured in a vial containing 10 mL of the selected organic solvent. The mixture was then ultra-sonicated (UP400S from Hielscher) for 10 min at full power (400 W, frequency of 24 kHz) dipping the vial in an ice bath to prevent solvent evaporation during sonication.

For the determination of the resistive behavior as a function of the temperature, one aliquot (20 µL) of rGO and TPSA-rGO dispersions in chloroform was drop-cast on gold plated electrodes supported on a Kapton® film (for solid support size details refer to [67]) and then left to evaporate at room temperature. The electrical resistance was measured at different temperatures in the range 20–60 °C as previously reported [68,69]. The measured resistances were obtained as a mean from one hundred measurements as allowed by the multimeter settings (KEITHLEY 2010, Tektronix, Beaverton, OR, USA).

For the determination of the resistive behavior as a function of the exposure to volatile organic compounds, the aliquot was drop-cast onto gold electrodes supported on an integrated device provided by Cad Line Pisa (Italy). The setup of the experiment as well as electrodes size and geometry were detailed reported in the recent literature [70,71]. Briefly, for each deposition THF, CHCl₃, and hexane (HEX) were tested. To account for the sensitivity of the devices, dispersions were exposed to an increasing amount of solvent. About 23 µL of solvent, i.e., corresponding to 5 ppm of the volume chamber was dropped by using a Gilson pipette and quickly the hole was closed with a rubber septum. Resistance values were taken every minute for a total of twenty and afterwards a new addition of 5 ppm was done until 50 ppm was reached.

2.4. Characterization

ATR-FT-IR spectra were recorded by means of a Perkin-Elmer Spectrum One (San Francisco, CA, USA), within the 4000–650 cm⁻¹ and averaged over 32 scans.

Scanning transmission electron microscopy (STEM, Thermo Fisher Scientific, Hillsboro, OR, USA) was performed on rGO samples using a FEI Quanta 450 equipped with a field emission gun. Particle analysis was performed using the public domain ImageJ 1.52k software (National Institutes of Health, Bethesda,

MD, USA). SEM images were acquired with a Dual Beam FIB/SEM Helios Nano-Lab 600i (Thermo Fisher Scientific), 5 kV accelerating voltage, and variable magnification. For SEM imaging, the samples were acquired without any additional preparation.

Image and confocal profilometry data were acquired with a Leica DCM 3D Confocal Profilometer (Leica Microsystems CMS GmbH, Mannheim, Germany).

The UV–vis spectra were recorded with a Perkin Elmer Lambda 650 spectrophotometer (San Francisco, CA, USA) using quartz cuvettes with an optical path of 1 cm.

Thermal degradation of rGO was analyzed via thermogravimetric analysis (TGA) with a Mettler Toledo TGA/SDTA851 instrument (Mettler Toledo, Columbus, OH, USA) under nitrogen flux (80 mL/min). All samples were tested in agreement with procedures previously reported [72].

Raman spectroscopy has been performed using a Horiba Jobin Yvon Xplora ONE confocal Raman microscope (Horiba Scientific, Horiba Italy, Roma, Italy). The wavelength of the excitation laser was 532 nm and the power of the laser was kept below 1 mW (at the objective) to avoid sample heating.

The electrical measurements of the rGO and TPSA-rGO solid dispersions were carried out according to literature reports [67,68,73,74].

XPS analysis was performed as described in [75]. Briefly, dried powder of TPSA-rGO and rGO were placed on a sample support and inserted in an ultra-high vacuum (UHV) analysis chamber (pressure 5×10^{-8}). The chamber was equipped with a VSW-TA10 X-ray source and a VSW-HA100 hemispherical analyzer with a 16-channel detector. The X-ray non-monochromatic source (Mg K α radiation, 1253.6 eV) was operated at 100 W (10 kV and 10 mA). XPS analysis was carried out to determine the intensity of each component using CasaXPS software (Casa Software Ltd., Teignmouth TQ14 8DE, UK) and correcting the extracted areas using the atomic sensitivity factors [75].

3. Result and Discussion

3.1. Dispersion of Reduced Graphene Oxide (rGO) in Organic Solvents

The production of stable graphene dispersion is of paramount importance for the fabrication of graphene-based devices and composites. We evaluated the dispersion of pristine rGO in five different apolar and polar aprotic organic solvents such as chloroform (CHCl₃), 1-methyl-2-pyrrolidone (NMP), hexane (HEX), tetrahydrofuran (THF), and toluene (TOL) (Figure 2). The dispersions were prepared by adding 5 mg of rGO in 10 mL of solvent and sonicated for 10 min. As reported, NMP is an excellent solvent to disperse rGO due to its high polarity (3.75 D) and surface energy (40.1 mN/m) similar to rGO [76,77]. Its dispersion showed a high value of absorbance (Abs > 4, inset Figure 2A) with evidence of signal saturation and absence of precipitates (Figure 2B). On the other hand, rGO displayed poor dispersibility in THF and in the non-polar TOL and HEX in agreement with the required combination of solvent polarity and surface energy [78]. In line with these findings, CHCl₃ showed a better dispersibility than these last solvents, possibly due to the generation of effective hydrogen bonding interactions between the residual functional groups of rGO and the chlorinated solvent [78].

An effective dispersion should also remain stable over a reasonable period of time. Therefore, the stability of rGO dispersions was evaluated after one month from the preparation (Supplementary Figure S1). rGO was found to retain its excellent dispersability in NMP, as expected. Conversely, TOL, THF, and HEX showed poor stability with time, whereas notwithstanding the similar UV–vis absorption spectrum in CHCl₃, partial sedimentation of rGO was found after one month.

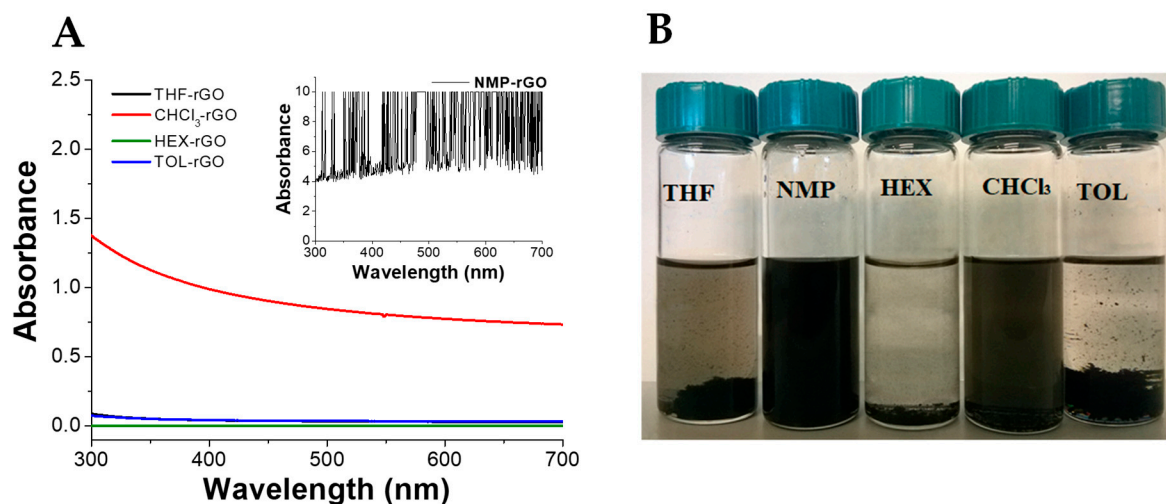


Figure 2. (A) UV-vis spectra and (B) optical pictures of rGO dispersed in organic solvent after preparation. Tetrahydrofuran (THF), 1-methyl-2-pyrrolidone (NMP), hexane (HEX), chloroform (CHCl₃), and toluene (TOL). For all dispersions, 5 mg of rGO in 10 mL of solvent.

The morphology of the rGO dispersion in chloroform was analyzed by scanning transmission electron microscopy (STEM, Figure 3). rGO flakes had a surface size of $2.25 \pm 0.45 \mu\text{m}^2$ and most of them appeared as single sheets with an average thickness of $0.7 \pm 0.2 \mu\text{m}$, thus confirming the effectiveness of the selected dispersing method in providing well-exfoliated rGO layers.

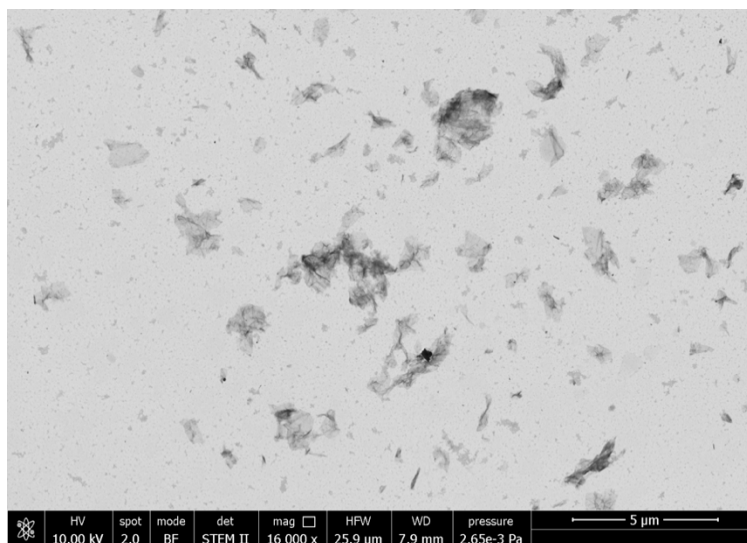


Figure 3. Scanning transmission electron microscopy (STEM) micrographs of rGO dispersed in chloroform.

3.2. rGO Functionalization with 3-(Dodecen-1-yl) Succinic Anhydride (TPSA) and Dispersion in Organic Solvents

rGO functionalized with 3-(dodecen-1-yl) succinic anhydride (TPSA-rGO) was prepared with the aim to enhance rGO dispersibility in organic solvents. The composition and structure of TPSA-rGO were characterized by thermogravimetric analysis (TGA), Raman, ATR-FTIR, XPS, and its morphology by scanning transmission electron microscopy (STEM). Figure 4A shows the ATR-FTIR spectra of rGO and TPSA-rGO. The former displays peaks of residual oxygen-functional groups C-O-C (1200 cm^{-1}) and C-O

stretching vibrations (1050 cm^{-1}). After its functionalization with TPSA, TPSA-rGO displays the typical stretching bands at 2922 cm^{-1} and 2852 cm^{-1} and bending at 1425 cm^{-1} and 1374 cm^{-1} attributed to the aliphatic C-H moieties of the attached alkyl chains. In addition, the significant contributions at 3500 , 1688 , and 1552 cm^{-1} were attributed to the presence of carboxylic groups that were possibly formed after the reaction of the succinic anhydride with the -OH residual groups of pristine rGO. Raman spectroscopy is also useful to investigate the structure of graphitic materials. The most diagnostic peaks in the Raman spectrum of graphene are the G and D bands, as evidenced in Figure 4B for rGO and TPSA-rGO samples [79,80]. The G-band centred at 1580 cm^{-1} represents the planar vibration of carbon atoms in most sp^2 graphitic materials. Conversely, the disorder-induced D-band at 1340 cm^{-1} is a result of scattering from defects that break the fundamental symmetry of the graphene sheet [81,82]. The significant contribution at 2900 cm^{-1} represents the combination of the first overtone of the D band (2D band) and the D + G band. Notably, the ratio of D and G bands peak intensities (I_D/I_G) can be used as a standard index to detect defects on the rGO layer. In this respect, the functionalization of rGO with TPSA inverted the intensities of the D and G-band and the I_D/I_G ratio of rGO and TPSA-rGO changed from 1.28 to 0.94, respectively. This unexpected feature has already been reported in the literature [83]. Aliphatic or aromatic functional groups in contact with the surface of the graphitic fillers effectively contribute to the generation of a more ordered structure, thus apparently limiting the extent of the structural disorder of the graphene layer.

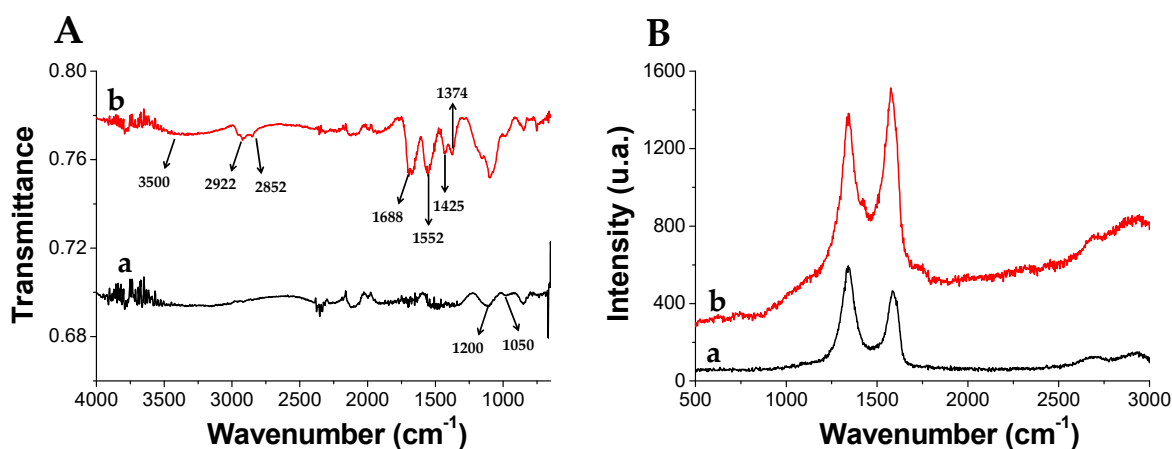


Figure 4. (A) FT-IR and (B) Raman spectra of (a) pristine rGO and (b) functionalized with TPSA (TPSA-rGO).

The functionalization of rGO with TPSA was also characterized by X-ray photoelectron spectroscopy (XPS). Figure 5 shows the XPS signals of C1s and O1s for the rGO and TPSA-rGO samples, whereas the percentage of each C1s and O1s components after signals deconvolution was reported in Table 1 [84]. Notably, TPSA-rGO displayed a marked decrease of carbon content in comparison to rGO, which was possibly attributed to the removal of the amorphous carbon during the functionalization process, or impurities physically adsorbed on the graphitic structure of rGO [75]. Nevertheless, the evident increase of the -C=O and COO ester or carboxylic acid contents formed after functionalization ratified the effective functionalization of rGO by TPSA. Precisely, COO increased from 3.4% to 5.2%, C-O from 10.1% to 11.3%, C=O 5.6% to 8.2%, and O=C from 11.6% to 12.0% (Table 1).

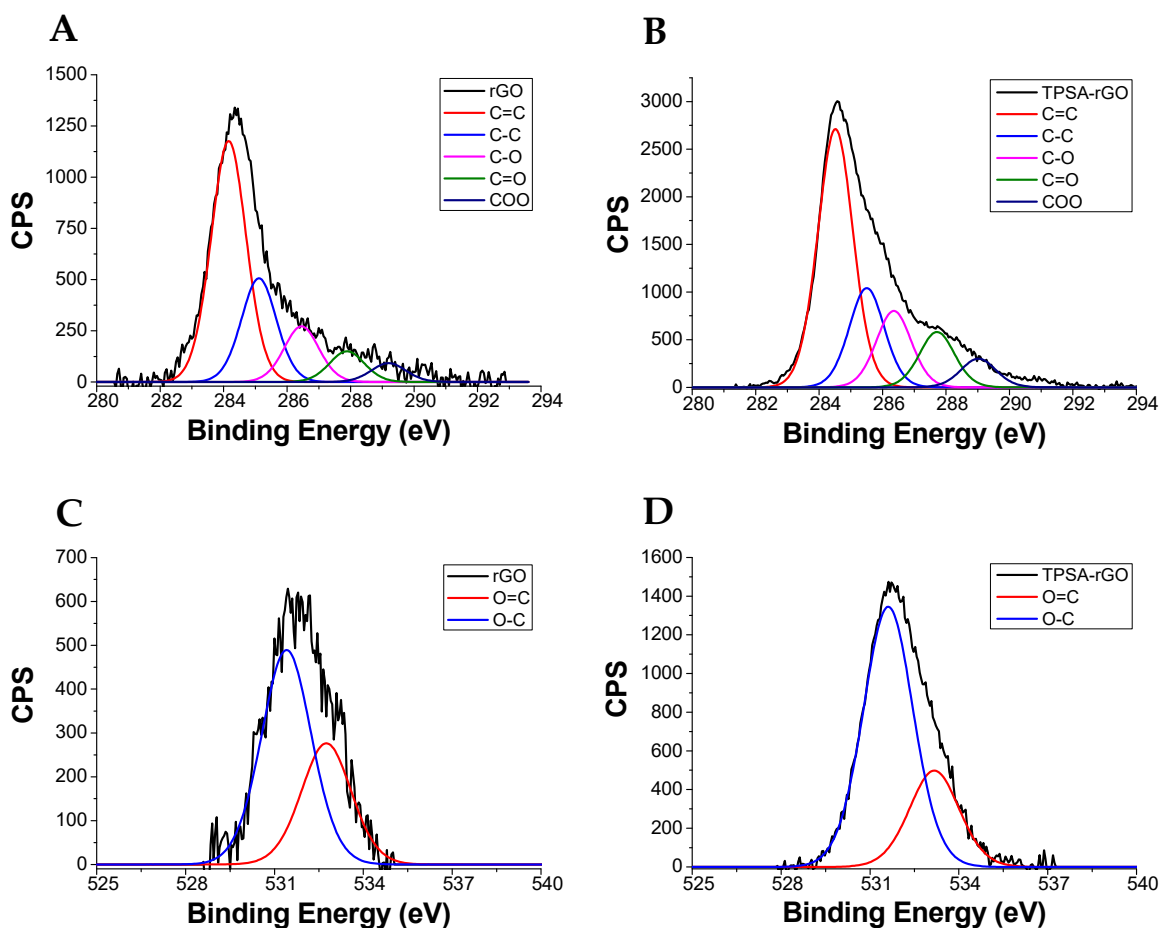


Figure 5. XPS profiles of C1s for (A) rGO and (B) TPSA-rGO, of O1s for (C) rGO and (D) TPSA-rGO.

Table 1. Components in rGO and TPSA-rGO as determined by XPS analysis.

Component	Position (eV)	rGO	TPSA-RGO
C=C	284.4	43.9%	38.3%
C-C	285.2	18.9%	15.7%
C-O	286.4	10.1%	11.3%
C=O	287.6	5.6%	8.2%
COO	289.0	3.4%	5.2%
C total	1432.6	81.9%	78.7%
O=C	533.0	11.6%	12.0%
O-C	531.0	6.5%	9.3%
O total	1064.0	18.1%	21.3%

We eventually evaluated the percentage of TPSA grafted onto rGO by thermogravimetric analysis (Figure 6). The experiments were carried out from 25 °C to 800 °C under nitrogen atmosphere. TPSA showed a thermal degradation at 260 °C with zero residual mass at 300 °C. rGO begun to degrade at about 300 °C with a gradual rate and without reaching a plateau even at 800 °C. The residual mass of the sample was calculated to be 87.1%. TPSA-rGO started to degrade before 300 °C due to the degradation of the grafted TPSA moieties and with an overall weight loss of 34% with respect to pristine rGO at 800 °C.

Therefore, the designed rGO functionalization process was able to graft more than 30% by weight of the alkyl succinic derivative.

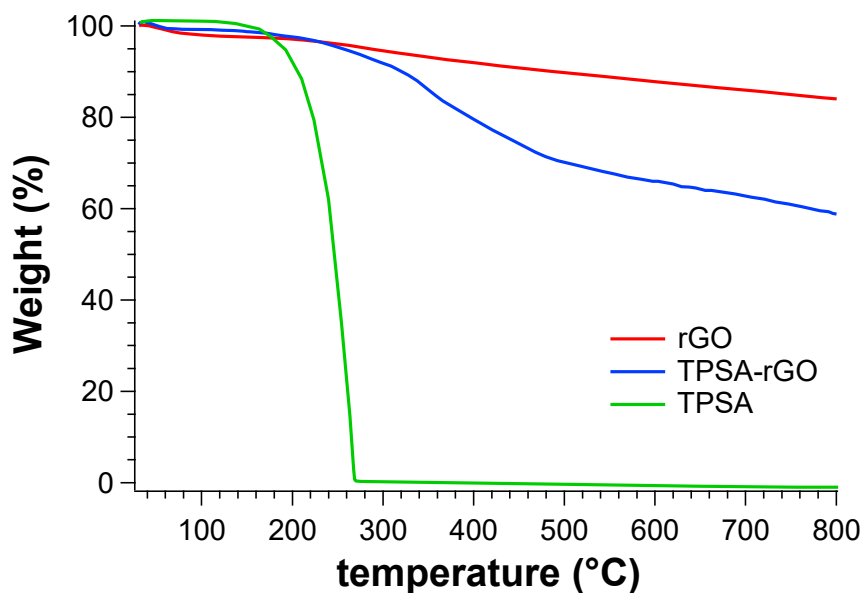


Figure 6. TGA analysis of TPSA, rGO, and TPSA-rGO.

We evaluated the dispersion of TPSA-rGO in the same five organic solvents as analogously investigated for pristine rGO to determine the effective contribution of the grafted TPSA moieties. The functionalization improves the rGO dispersion considerably in the organic solvents, except in hexane (Figure 7). TPSA-rGO dispersed in NMP, CHCl_3 , and THF showed very high values of absorbance and with clear evidence of signal saturation, i.e., indicating a substantial increase of the rGO dispersibility. This suggests that the incorporation of the $-\text{C}=\text{OOH}$ and $-\text{COO}$ alkyl groups of the graphitic surface of rGO substantially increase the number of effective interactions with the polar solvent molecules.

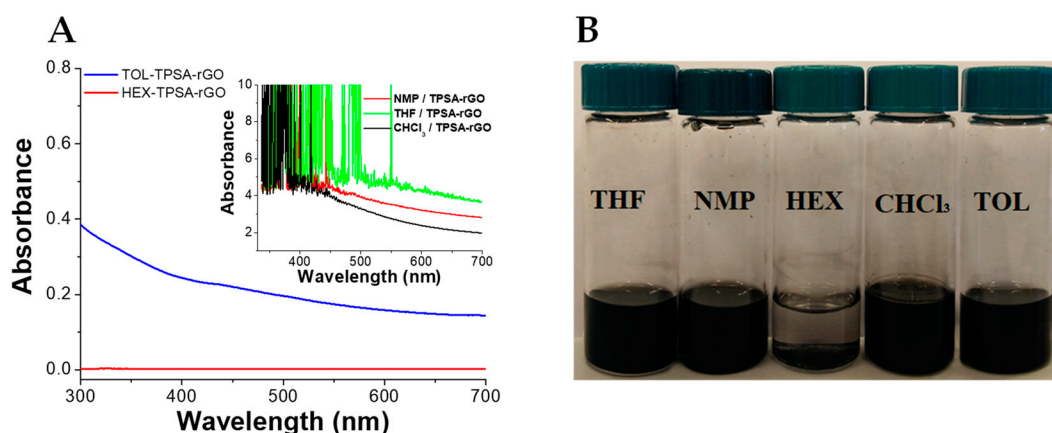


Figure 7. (A) UV-Vis spectra and (B) optical pictures of TPSA-rGO dispersed in organic solvent after preparation. Tetrahydrofuran (THF), 1-methyl-2-pyrrolidone (NMP), hexane (HEX), chloroform (CHCl_3), and toluene (TOL). For all dispersions, 5 mg of TPSA-rGO in 10 mL of solvent.

Moreover, by comparing the absorbance values of the rGO dispersed in toluene after and before the functionalization with TPSA (Figure S2), an overall four-fold increase in the amount of the graphitic

material contained in the mixture can be determined. This feature suggested that the grafted TPSA was also able to enhance the rGO dispersibility into an apolar aromatic solvent such as toluene. The presence of such effective interactions was eventually confirmed by analyzing the stability of the TPSA-rGO toluene dispersions after one month from the preparation. It was worth noting that the UV-vis absorption spectra recorded on the as-prepared sample was superimposable with that registered one month later (Figure S2).

TPSA-rGO dispersions were studied by STEM to evaluate if the chemical modification of rGO could adversely affect its morphology. Notably, both average surface size and thickness maintained unchanged after the modification with TPSA (Figure S3), thus suggesting that the designed functionalization process preserved the rGO main morphological characteristics.

3.3. Resistive Properties of TPSA-rGO and rGO as a Function of Temperature

As a semiconductor, the conductivity of a graphitic material increases upon heating, thus making it appropriate for use in small-size temperature sensors [68,69]. In connection with these findings, aliquots (20 μ L) of rGO and TPSA-rGO chloroform dispersions were drop-cast onto the electrodes on plastic support (Figure S4), and the electrical resistance of the derived films measured after the complete evaporation of the solvent. The measurements were carried out in replicate ($n = 3$). The substantial difference of the measured resistance of the two rGO samples at room temperature suggested a low reproducibility of the casting procedure, possibly attributed to the very heterogeneous chloroform mixtures [68]. On the contrary, the resistance values of the TPSA-rGO samples were in excellent agreement with values at least one order of magnitude below those of rGO (Table 2). Indeed, following the UV-Vis experiments, TPSA-rGO dispersions in chloroform contained a greater content of the graphitic material that was homogeneously distributed in the solid phase in very effective percolative structure (Figures S5–S7).

Table 2. Resistance of rGO and TPSA-rGO dispersed in chloroform as the average of three replicates \pm standard deviation.

Sample	Resistance (M Ω)
rGO 1	5.1 \pm 0.1
rGO 2	28 \pm 2
TPSA-rGO 1	0.58 \pm 0.05
TPSA-rGO 2	0.46 \pm 0.05

The resistance variation with temperature was then measured between 20 $^{\circ}$ C and 60 $^{\circ}$ C and over three successive heating-cooling cycles. The heterogeneous distribution of the rGO graphitic material in the sensor device was also reflected in the resistive behavior as a function of temperature variations (Figure 8A). The resistance of rGO decreased with the temperature according to the semiconducting behavior, but significant fluctuations of the measured data were collected (Figure 8B). Moreover, rGO 2 sample was discarded for further investigations since no variation of resistance was measured (data not shown). TPSA-rGO samples showed the same resistive behavior with temperature but a more reproducible resistance variation upon heating was gathered. These features were also confirmed by analyzing the replicate experiments over successive second and third heating scans. Notably, the linear trend was confirmed for the TPSA-rGO samples only and with a maximum resistance variation extent of about 20% (Figure 8C,D) within the temperature scan sequence.

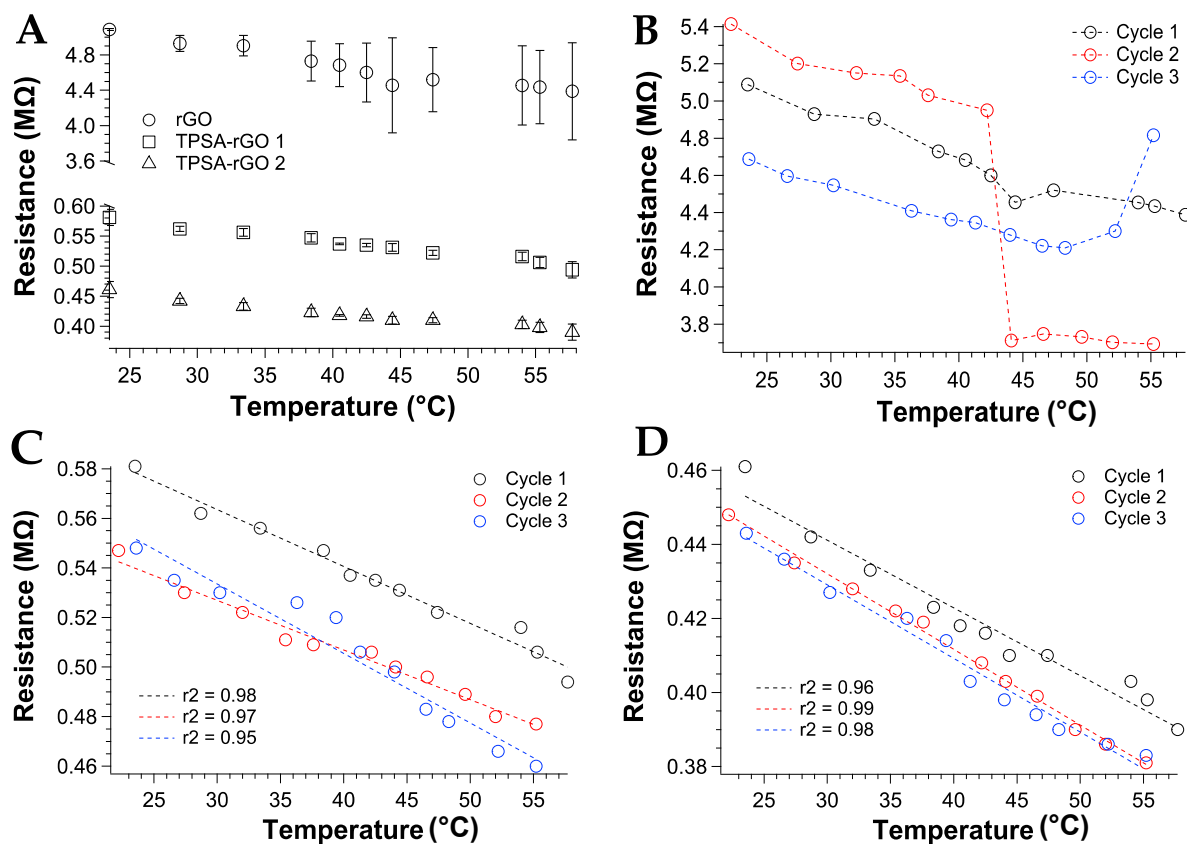


Figure 8. Resistance variation as a function of the temperature: (A) first heating cycle for rGO and TPSA-rGO samples; all heating cycles for (B) rGO, (C) TPSA-rGO 1 with linear interpolation, and (D) TPSA-rGO 2 with linear interpolation. As insets, the r^2 values of the linear fit were reported.

As a first-order approximation for the considered range, the temperature coefficient α_T of the TPSA-rGO samples can be calculated according to the Equation (1) [68].

$$\alpha_T = \frac{R_{final} - R_{initial}}{T_{final} - T_{initial}} / R_{initial} \quad (1)$$

where α is the temperature coefficient expressed in K^{-1} . Table 3 shows the sensitivity values obtained for each sample and cycles.

Table 3. Temperature coefficient α (K^{-1}).

Cycle	TPSA-rGO 1	TPSA-rGO 2
1	−0.004	−0.004
2	−0.004	−0.004
3	−0.005	−0.005

The TPSA-rGO samples displayed sensitivity corresponding to a negative α in the order of $10^{-3} K^{-1}$, i.e., comparable, as absolute value, to values found in metals [68,69]. The resistance measures have an excellent reproducibility of the temperature coefficient with a slight variation only in the last cycle, thus confirming the use of rGO percolative networks as small temperature sensors.

3.4. Resistive Properties of TPSA-rGO and rGO Exposed to Volatile Organic Solvents (VOCs)

The detection of volatile organic compounds at room temperature with fast response is of paramount importance for safety reasons. In graphene based-sensors, the solvent adsorbed by the graphitic material induces a variation in the electrical conductivity because of the effective perturbation of the percolative pathways [23,25,85]. Therefore, we fabricated a sensor device by depositing 100 μL of TPSA-rGO dispersed in chloroform on an electrical circuit and the electrical signal collected by a digital multimeter with a data logger (S8 and experimental). Notably, the dispersion was left drying in the air and then under a mechanical vacuum for about 4 h. The TPSA-rGO based-sensor was then exposed to the vapors of three different organic solvents such as THF, CHCl_3 , and HEX inside of a sealed chamber (S9). THF and CHCl_3 were selected as potentially interacting solvents with TPSA-rGO, whereas HEX was investigated being a very volatile solvent but barely interacting with the graphitic compound. Figure 9 shows the increase of the resistance of the sensors as it was exposed to different vapor concentrations. In particular, the sensor appeared to respond linearly as the concentration of THF and CHCl_3 increased. Notably, for both THF and CHCl_3 , the device starts to become sensitive for VOC concentration higher than 5–10 ppm. In the case of HEX, the electrical resistance of the sensor did not substantially change within the investigated interval of concentrations, which again confirmed the weak interaction between the functionalized rGO and the aliphatic hydrocarbon solvent.

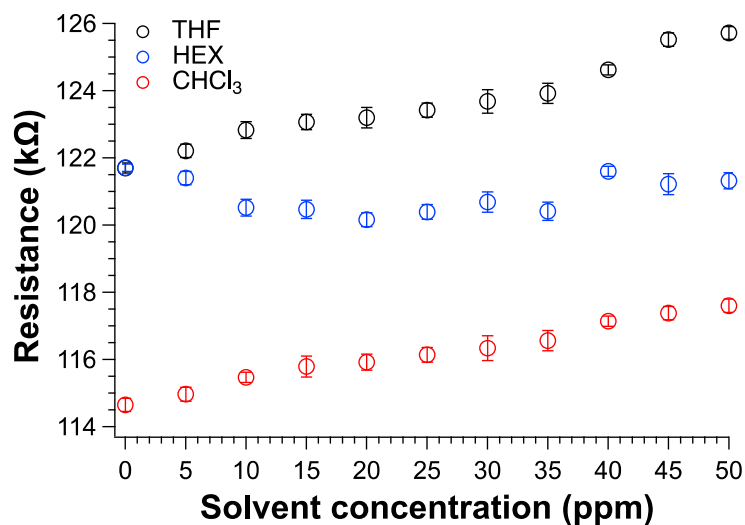


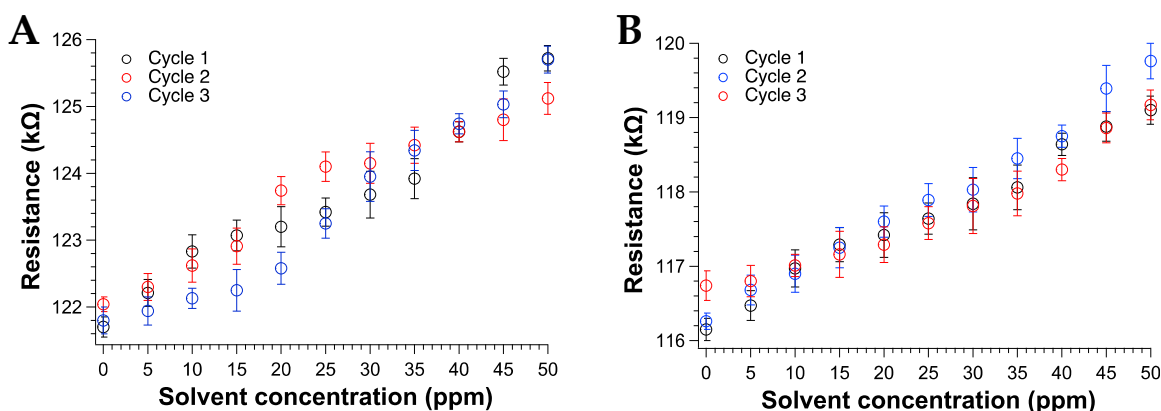
Figure 9. Resistance variation of TPSA-rGO as a function of VOC concentration expressed in ppm.

We evaluated the sensor performances for each solvent by comparing their Pearson's correlation coefficients (PCC) [86] (Table 4). PCC measures the statistical relationship between two continuous variables that were the sensor resistance and the concentration of the solvent vapors in ppm in our case. PCC values range from +1 to -1, where +1 designates a perfect positive relationship, -1 indicates a perfect negative relationship, and a 0 suggests that no relationship exists between the two variables. The experiment carried out with HEX gathered a PCC close to zero, thus indicating the very low sensibility of the device towards the hydrocarburic vapor molecules. In contrast, CHCl_3 and THF achieved a PCC very close to one thanks to the noteworthy sensibility of the TPSA-rGO based-sensor towards volatile and polar compounds.

Table 4. Pearson correlation coefficient of the resistance variation in function of the solvent.

Solvent	Pearson Correlation Coefficient
THF	0.90
HEX	0.05
CHCl ₃	0.90

We also assessed the reproducibility of the sensor response to THF and CHCl₃ vapors after three absorption–desorption cycles. Notably, after VOCs exposure, the sample was placed under a high vacuum (about 0.1 mm Hg for about 4 h) to ensure the total desorption of the adsorbed molecules from the sensing surface. Figure 10 reports the percentage variation of the resistance ($\Delta R/R_0$, with R_0 the resistance before vapor exposure), after each cycle for THF and CHCl₃.

**Figure 10.** Responses curves of the TPSA-RGO based-sensors as a function of (A) THF (B) CHCl₃ vapors concentration (ppm).

According to the data, the sensor displayed an excellent response to THF and CHCl₃ vapors, especially at low ppm content [87,88] and comparable to the best performances found in the recent literature [89]. The 0.5% of fluctuation of the sensor output recorded at 0 ppm of chloroform exposure (Figure 10b) was attributed to a uncomplete drying procedure of the sensor after the second cycle. Nevertheless, such issue did not influence the overall response even during the third cycle of CHCl₃ exposure. Notably, the sensing response of the TPSA-rGO based-sensor towards THF appeared statistically the same of that displayed towards CHCl₃ although a certain superior resistance variation could be appreciated for the former VOC (Figure 11). This feature was not totally unexpected due to the higher affinity of THF with TPSA-rGO, as demonstrated by the UV–Vis experiments reported in Figure 7A.

Also, the TPSA-rGO based-device displayed a good reproducibility of the sensing response, as eventually confirmed by the calculated sensitivity coefficient α (defined as $(\Delta R/R_0)/\Delta$ solvent concentration) reported in Table 5.

Table 5. Sensitivity α (ppm^{−1}) of the sensor to THF and CHCl₃. Standard deviation of 0.0001 for all data.

Cycle	Chloroform	Tetrahydrofuran
1	0.0004	0.0006
2	0.0005	0.0005
3	0.0004	0.0006

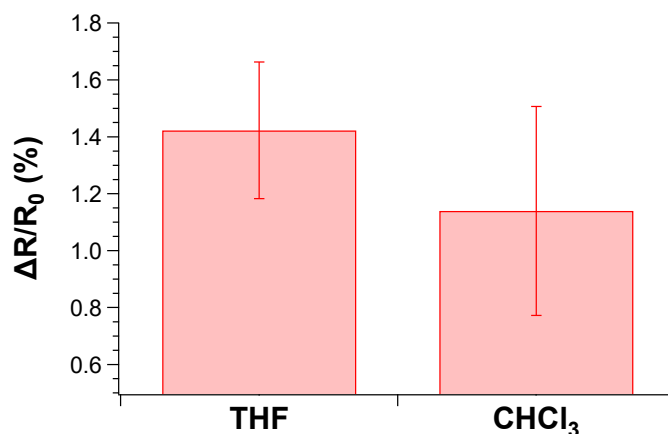


Figure 11. Comparison of responses from the sensing elements to the 25 ppm VOCs.

From these data, the detection limit of the sensor (LOD) can be determined. LOD can be effectively expressed as the standard deviation of the blank signal (σ_0) (in absence of stimulus, or in standard condition), divided for the sensitivity and multiplied for a confidence factor that is typically defined as 3.29 (corresponding to a confidence level of 99%) and according to the Equation (2) [90].

$$LOD = \frac{3.29 \cdot \sigma_0}{S} \quad (2)$$

In our case, $\sigma_0 = 0.0018$ (calculated as standard deviation of $\Delta R/R_0$) for CHCl_3 (sensitivity = 0.0004 ppm^{-1}) and $\sigma_0 = 0.0020$ for THF (sensitivity = 0.0006 ppm^{-1}), thus obtaining a detection limit of 15 ppm and 11 ppm, respectively.

4. Conclusions

We have shown that rGO can be effectively functionalized with TPSA (rGO-TPSA) thanks to the residual reactive oxygenated moieties of the former and the succinic groups of the latter. The amount of grafted TPSA of about 30 wt % determined by qualitative and quantitative investigation analyses (TGA, XPS, and FTIR-ATR) strongly enhanced rGO dispersibility in the investigated organic solvents with the only exception of hexane due to its completely apolar and hydrocarburic nature. The graphitic characteristics of the rGO layer remained almost unchanged after functionalization, which allowed the realization of solid dispersions of TPSA-rGO with a reproducible electrical response towards temperature solicitations (negative temperature coefficient of 10^{-3} K^{-1}) and against the exposure to THF and CHCl_3 vapors. In this case, TPSA-rGO showed electrical resistance variation with a detection limit in the order of 10 ppm and sensitivity α of about 10^{-4} ppm^{-1} . Notably, the sensor did not respond to the hexane vapors, thus confirming the weak chemical interaction of the solvent with the functionalized graphene layer.

Supplementary Materials: The following are available online at <http://www.mdpi.com/2227-9040/8/2/43/s1>. Figure S1. (A) UV–Vis spectra and (B) optical pictures of rGO dispersed in organic solvent after one month. Figure S2. UV–Vis spectra of TPSA-rGO and rGO dispersed in toluene (TOL) after preparation and after one month. Figure S3. Scanning transmission electron microscopy (STEM) micrographs of TPSA-rGO dispersed in chloroform. Figure S4. Temperature device electrodes and main characteristics. Figure S5. SEM images of temperature device electrodes. Figure S6. Optical and confocal profilometry of temperature device coated with rGO at different locations and at different magnifications. Figure S7. Optical and confocal profilometry of temperature device coated with TPSA-rGO at different locations and at different magnifications. Figure S8. Organic solvent vapors device and main characteristics. Figure S9. Organic solvent vapors chamber and main characteristics.

Author Contributions: Conceptualization, A.P.; Methodology, M.M.; Data curation, E.A.-H., A.P. and V.M.; Writing—original draft preparation, E.A.-H.; Writing—review and editing, A.P. and V.M.; Funding acquisition, V.M. All authors have read and agreed to the published version of the manuscript.

Funding: This research received no external funding.

Acknowledgments: CISUP—Centre for Instrumentation Sharing-University of Pisa is kindly acknowledged for STEM measurements.

Conflicts of Interest: The authors declare no conflict of interest.

References

- Novoselov, K.S.; Geim, A.K.; Morozov, S.V.; Jiang, D.; Zhang, Y.; Dubonos, S.V.; Grigorieva, I.V.; Firsov, A.A. Electric field effect in atomically thin carbon films. *Science* **2004**, *306*, 666. [[CrossRef](#)]
- Meyer, J.C.; Geim, A.K.; Katsnelson, M.I.; Novoselov, K.S.; Booth, T.J.; Roth, S. The structure of suspended graphene sheets. *Nature* **2007**, *446*, 60–63. [[CrossRef](#)] [[PubMed](#)]
- Ferrari, A.C.; Bonaccorso, F.; Fal'ko, V.; Novoselov, K.S.; Roche, S.; Bøggild, P.; Borini, S.; Koppens, F.H.L.; Palermo, V.; Pugno, N.; et al. Science and technology roadmap for graphene, related two-dimensional crystals, and hybrid systems. *Nanoscale* **2015**, *7*, 4598–4810. [[CrossRef](#)] [[PubMed](#)]
- Peres, N.M.R. Graphene, new physics in two dimensions. *Europhys. News* **2009**, *40*, 17–20. [[CrossRef](#)]
- Hone, J.; Whitney, M.; Piskoti, C.; Zettl, A. Thermal conductivity of single-walled carbon nanotubes. *Phys. Rev. B* **1999**, *59*, R2514–R2516. [[CrossRef](#)]
- Lee, C.; Wei, X.; Kysar, J.W.; Hone, J. Measurement of the elastic properties and intrinsic strength of monolayer graphene. *Science* **2008**, *321*, 385. [[CrossRef](#)] [[PubMed](#)]
- Bao, W.; Miao, F.; Chen, Z.; Zhang, H.; Jang, W.; Dames, C.; Lau, C.N. Controlled ripple texturing of suspended graphene and ultrathin graphite membranes. *Nat. Nanotechnol.* **2009**, *4*, 562–566. [[CrossRef](#)]
- Nair, R.R.; Blake, P.; Grigorenko, A.N.; Novoselov, K.S.; Booth, T.J.; Stauber, T.; Peres, N.M.R.; Geim, A.K. Fine structure constant defines visual transparency of graphene. *Science* **2008**, *320*, 1308. [[CrossRef](#)]
- Zhang, K.; Zhang, L.L.; Zhao, X.S.; Wu, J. Graphene/polyaniline nanofiber composites as supercapacitor electrodes. *Chem. Mater.* **2010**, *22*, 1392–1401. [[CrossRef](#)]
- Stoller, M.D.; Park, S.; Zhu, Y.; An, J.; Ruoff, R.S. Graphene-based ultracapacitors. *Nano Lett.* **2008**, *8*, 3498–3502. [[CrossRef](#)]
- Pal, N.; Dubey, P.; Gopinath, P.; Pal, K. Combined effect of cellulose nanocrystal and reduced graphene oxide into poly-lactic acid matrix nanocomposite as a scaffold and its anti-bacterial activity. *Int. J. Biol. Macromol.* **2017**, *95*, 94–105. [[CrossRef](#)] [[PubMed](#)]
- Kymakis, E.; Savva, K.; Stylianakis, M.M.; Fotakis, C.; Stratakis, E. Flexible organic photovoltaic cells with in situ nonthermal photoreduction of spin-coated graphene oxide electrodes. *Adv. Funct. Mater.* **2013**, *23*, 2742–2749. [[CrossRef](#)]
- Lu, C.-H.; Yang, H.-H.; Zhu, C.-L.; Chen, X.; Chen, G.-N. A graphene platform for sensing biomolecules. *Angew. Chem. Int. Ed.* **2009**, *48*, 4785–4787. [[CrossRef](#)] [[PubMed](#)]
- Bae, S.; Kim, H.; Lee, Y.; Xu, X.; Park, J.-S.; Zheng, Y.; Balakrishnan, J.; Lei, T.; Ri Kim, H.; Song, Y.I.; et al. Roll-to-roll production of 30-inch graphene films for transparent electrodes. *Nat. Nanotechnol.* **2010**, *5*, 574–578. [[CrossRef](#)] [[PubMed](#)]
- Yoonessi, M.; Shi, Y.; Scheiman, D.A.; Lebron-Colon, M.; Tigelaar, D.M.; Weiss, R.A.; Meador, M.A. Graphene polyimide nanocomposites; Thermal, mechanical, and high-temperature shape memory effects. *ACS Nano* **2012**, *6*, 7644–7655. [[CrossRef](#)] [[PubMed](#)]
- Mendes, G.R.; Wróbel, S.P.; Bachmatiuk, A.; Sun, J.; Gemming, T.; Liu, Z.; Rummeli, H.M. Carbon nanostructures as a multi-functional platform for sensing applications. *Chemosensors* **2018**, *6*, 60. [[CrossRef](#)]
- Dong, X.M.; Fu, R.W.; Zhang, M.Q.; Zhang, B.; Rong, M.Z. Electrical resistance response of carbon black filled amorphous polymer composite sensors to organic vapors at low vapor concentrations. *Carbon* **2004**, *42*, 2551–2559. [[CrossRef](#)]

18. Yoon, H.J.; Jun, D.H.; Yang, J.H.; Zhou, Z.; Yang, S.S.; Cheng, M.M.-C. Carbon dioxide gas sensor using a graphene sheet. *Sens. Actuators B Chem.* **2011**, *157*, 310–313. [\[CrossRef\]](#)
19. Lu, G.; Ocola, L.E.; Chen, J. Gas detection using low-temperature reduced graphene oxide sheets. *Appl. Phys. Lett.* **2009**, *94*, 083111. [\[CrossRef\]](#)
20. Pearce, R.; Iakimov, T.; Andersson, M.; Hultman, L.; Spetz, A.L.; Yakimova, R. Epitaxially grown graphene based gas sensors for ultra sensitive NO₂ detection. *Sens. Actuators B Chem.* **2011**, *155*, 451–455. [\[CrossRef\]](#)
21. Yavari, F.; Castillo, E.; Gullapalli, H.; Ajayan, P.M.; Koratkar, N. High sensitivity detection of NO₂ and NH₃ in air using chemical vapor deposition grown graphene. *Appl. Phys. Lett.* **2012**, *100*, 203120. [\[CrossRef\]](#)
22. Schedin, F.; Geim, A.K.; Morozov, S.V.; Hill, E.W.; Blake, P.; Katsnelson, M.I.; Novoselov, K.S. Detection of individual gas molecules adsorbed on graphene. *Nat. Mater.* **2007**, *6*, 652–655. [\[CrossRef\]](#) [\[PubMed\]](#)
23. Liu, H.; Huang, W.; Yang, X.; Dai, K.; Zheng, G.; Liu, C.; Shen, C.; Yan, X.; Guo, J.; Guo, Z. Organic vapor sensing behaviors of conductive thermoplastic polyurethane–graphene nanocomposites. *J. Mater. Chem. C* **2016**, *4*, 4459–4469. [\[CrossRef\]](#)
24. Ko, G.; Kim, H.Y.; Ahn, J.; Park, Y.M.; Lee, K.Y.; Kim, J. Graphene-based nitrogen dioxide gas sensors. *Curr. Appl. Phys.* **2010**, *10*, 1002–1004. [\[CrossRef\]](#)
25. Wu, Z.; Chen, X.; Zhu, S.; Zhou, Z.; Yao, Y.; Quan, W.; Liu, B. Enhanced sensitivity of ammonia sensor using graphene/polyaniline nanocomposite. *Sens. Actuators B Chem.* **2013**, *178*, 485–493. [\[CrossRef\]](#)
26. Geim, A.K. Graphene: Status and prospects. *Science* **2009**, *324*, 1530. [\[CrossRef\]](#)
27. Dai, L. Functionalization of graphene for efficient energy conversion and storage. *Acc. Chem. Res.* **2013**, *46*, 31–42. [\[CrossRef\]](#)
28. Li, X.; Zhu, Y.; Cai, W.; Borysiak, M.; Han, B.; Chen, D.; Piner, R.D.; Colombo, L.; Ruoff, R.S. Transfer of large-area graphene films for high-performance transparent conductive electrodes. *Nano Lett.* **2009**, *9*, 4359–4363. [\[CrossRef\]](#)
29. Ratnac, K.R.; Yang, W.; Ringer, S.P.; Braet, F. Toward ubiquitous environmental gas sensors—Capitalizing on the promise of graphene. *Environ. Sci. Technol.* **2010**, *44*, 1167–1176. [\[CrossRef\]](#)
30. Shams, S.S.; Ruoyu, Z.; Jin, Z. Graphene synthesis: A review. *Mater. Sci. Pol.* **2015**, *33*, 566–578. [\[CrossRef\]](#)
31. Eizenberg, M.; Blakely, J.M. Carbon monolayer phase condensation on Ni(111). *Surf. Sci.* **1979**, *82*, 228–236. [\[CrossRef\]](#)
32. Kim, K.S.; Zhao, Y.; Jang, H.; Lee, S.Y.; Kim, J.M.; Kim, K.S.; Ahn, J.-H.; Kim, P.; Choi, J.-Y.; Hong, B.H. Large-scale pattern growth of graphene films for stretchable transparent electrodes. *Nature* **2009**, *457*, 706–710. [\[CrossRef\]](#) [\[PubMed\]](#)
33. Amini, S.; Garay, J.; Liu, G.; Balandin, A.A.; Abbaschian, R. Growth of large-area graphene films from metal-carbon melts. *J. Appl. Phys.* **2010**, *108*, 094321. [\[CrossRef\]](#)
34. Sutter, P. How silicon leaves the scene. *Nat. Mater.* **2009**, *8*, 171–172. [\[CrossRef\]](#) [\[PubMed\]](#)
35. Novoselov, K.S. Nobel lecture: Graphene: Materials in the flatland. *Rev. Mod. Phys.* **2011**, *83*, 837–849. [\[CrossRef\]](#)
36. Zhan, D.; Sun, L.; Ni, Z.H.; Liu, L.; Fan, X.F.; Wang, Y.; Yu, T.; Lam, Y.M.; Huang, W.; Shen, Z.X. FeCl₃-based few-layer graphene intercalation compounds: Single linear dispersion electronic band structure and strong charge transfer doping. *Adv. Funct. Mater.* **2010**, *20*, 3504–3509. [\[CrossRef\]](#)
37. Borah, M.; Dahiya, M.; Sharma, S.; Mathur, R.B.; Dhakate, S.R. Few layer graphene derived from wet ball milling of expanded graphite and few layer graphene based polymer composite. *Mater. Focus* **2014**, *3*, 300–309. [\[CrossRef\]](#)
38. Ranjan, P.; Agrawal, S.; Sinha, A.; Rao, T.R.; Balakrishnan, J.; Thakur, A.D. A low-cost non-explosive synthesis of graphene oxide for scalable applications. *Sci. Rep.* **2018**, *8*, 12007. [\[CrossRef\]](#)
39. Paredes, J.I.; Villar-Rodil, S.; Martínez-Alonso, A.; Tascón, J.M.D. Graphene oxide dispersions in organic solvents. *Langmuir* **2008**, *24*, 10560–10564. [\[CrossRef\]](#)
40. Brodie, B.C. XIII. On the atomic weight of graphite. *Philos. Trans. R. Soc. Lond.* **1859**, *149*, 249–259. [\[CrossRef\]](#)
41. Staudenmaier, L. Verfahren zur darstellung der graphitsäure. *Ber. Der Dtsch. Chem. Ges.* **1898**, *31*, 1481–1487. [\[CrossRef\]](#)
42. Hummers, W.S.; Offeman, R.E. Preparation of graphitic oxide. *J. Am. Chem. Soc.* **1958**, *80*, 1339. [\[CrossRef\]](#)
43. Boukhvalov, D.W.; Katsnelson, M.I. Modeling of graphite oxide. *J. Am. Chem. Soc.* **2008**, *130*, 10697–10701. [\[CrossRef\]](#) [\[PubMed\]](#)

44. Li, D.; Kaner, R.B. Graphene-based materials. *Science* **2008**, *320*, 1170. [[CrossRef](#)] [[PubMed](#)]
45. Stankovich, S.; Piner, R.D.; Chen, X.; Wu, N.; Nguyen, S.T.; Ruoff, R.S. Stable aqueous dispersions of graphitic nanoplatelets via the reduction of exfoliated graphite oxide in the presence of poly(sodium 4-styrenesulfonate). *J. Mater. Chem.* **2006**, *16*, 155–158. [[CrossRef](#)]
46. Gudarzi, M.M.; Moghadam, M.H.M.; Sharif, F. Spontaneous exfoliation of graphite oxide in polar aprotic solvents as the route to produce graphene oxide—Organic solvents liquid crystals. *Carbon* **2013**, *64*, 403–415. [[CrossRef](#)]
47. Mann, J.A.; Dichtel, W.R. Noncovalent functionalization of graphene by molecular and polymeric adsorbates. *J. Phys. Chem. Lett.* **2013**, *4*, 2649–2657. [[CrossRef](#)]
48. Dasari Shareena, T.P.; McShan, D.; Dasmahapatra, A.K.; Tchounwou, P.B. A review on graphene-based nanomaterials in biomedical applications and risks in environment and health. *Nano Micro Lett.* **2018**, *10*, 53. [[CrossRef](#)]
49. Stankovich, S.; Dikin, D.A.; Piner, R.D.; Kohlhaas, K.A.; Kleinhammes, A.; Jia, Y.; Wu, Y.; Nguyen, S.T.; Ruoff, R.S. Synthesis of graphene-based nanosheets via chemical reduction of exfoliated graphite oxide. *Carbon* **2007**, *45*, 1558–1565. [[CrossRef](#)]
50. Wang, G.; Yang, J.; Park, J.; Gou, X.; Wang, B.; Liu, H.; Yao, J. Facile synthesis and characterization of graphene nanosheets. *J. Phys. Chem. C* **2008**, *112*, 8192–8195. [[CrossRef](#)]
51. McAllister, M.J.; Li, J.-L.; Adamson, D.H.; Schniepp, H.C.; Abdala, A.A.; Liu, J.; Herrera-Alonso, M.; Milius, D.L.; Car, R.; Prud'homme, R.K.; et al. single sheet functionalized graphene by oxidation and thermal expansion of graphite. *Chem. Mater.* **2007**, *19*, 4396–4404. [[CrossRef](#)]
52. Fan, H.; Wang, L.; Zhao, K.; Li, N.; Shi, Z.; Ge, Z.; Jin, Z. Fabrication, mechanical properties, and biocompatibility of graphene-reinforced chitosan composites. *Biomacromolecules* **2010**, *11*, 2345–2351. [[CrossRef](#)]
53. Xu, Y.; Bai, H.; Lu, G.; Li, C.; Shi, G. Flexible Graphene films via the filtration of water-soluble noncovalent functionalized graphene sheets. *J. Am. Chem. Soc.* **2008**, *130*, 5856–5857. [[CrossRef](#)] [[PubMed](#)]
54. Gilje, S.; Han, S.; Wang, M.; Wang, K.L.; Kaner, R.B. A chemical route to graphene for device applications. *Nano Lett.* **2007**, *7*, 3394–3398. [[CrossRef](#)]
55. Dikin, D.A.; Stankovich, S.; Zimney, E.J.; Piner, R.D.; Dommett, G.H.B.; Evmenenko, G.; Nguyen, S.T.; Ruoff, R.S. Preparation and characterization of graphene oxide paper. *Nature* **2007**, *448*, 457–460. [[CrossRef](#)] [[PubMed](#)]
56. Niyogi, S.; Bekyarova, E.; Itkis, M.E.; McWilliams, J.L.; Hamon, M.A.; Haddon, R.C. Solution properties of graphite and graphene. *J. Am. Chem. Soc.* **2006**, *128*, 7720–7721. [[CrossRef](#)]
57. Gómez-Navarro, C.; Weitz, R.T.; Bittner, A.M.; Scolari, M.; Mews, A.; Burghard, M.; Kern, K. Electronic transport properties of individual chemically reduced graphene oxide sheets. *Nano Lett.* **2007**, *7*, 3499–3503. [[CrossRef](#)]
58. Eda, G.; Lin, Y.-Y.; Miller, S.; Chen, C.-W.; Su, W.-F.; Chhowalla, M. Transparent and conducting electrodes for organic electronics from reduced graphene oxide. *Appl. Phys. Lett.* **2008**, *92*, 233305. [[CrossRef](#)]
59. Wang, X.; Zhi, L.; Müllen, K. Transparent, conductive graphene electrodes for dye-sensitized solar cells. *Nano Lett.* **2008**, *8*, 323–327. [[CrossRef](#)]
60. Becerril, H.A.; Mao, J.; Liu, Z.; Stoltenberg, R.M.; Bao, Z.; Chen, Y. Evaluation of solution-processed reduced graphene oxide films as transparent conductors. *ACS Nano* **2008**, *2*, 463–470. [[CrossRef](#)]
61. Lipatov, A.; Varezchnikov, A.; Wilson, P.; Sysoev, V.; Kolmakov, A.; Sinitiskii, A. Highly selective gas sensor arrays based on thermally reduced graphene oxide. *Nanoscale* **2013**, *5*, 5426–5434. [[CrossRef](#)] [[PubMed](#)]
62. Dua, V.; Surwade, S.P.; Ammu, S.; Agnihotra, S.R.; Jain, S.; Roberts, K.E.; Park, S.; Ruoff, R.S.; Manohar, S.K. All-organic vapor sensor using inkjet-printed reduced graphene oxide. *Angew. Chem. Int. Ed.* **2010**, *49*, 2154–2157. [[CrossRef](#)] [[PubMed](#)]
63. Lu, G.; Park, S.; Yu, K.; Ruoff, R.S.; Ocola, L.E.; Rosenmann, D.; Chen, J. Toward practical gas sensing with highly reduced graphene oxide: A new signal processing method to circumvent run-to-run and device-to-device variations. *ACS Nano* **2011**, *5*, 1154–1164. [[CrossRef](#)]
64. Hasan, N.; Zhang, W.; Radadia, A.D. Few-flakes reduced graphene oxide sensors for organic vapors with a high signal-to-noise ratio. *Nanomaterials* **2017**, *7*, 339. [[CrossRef](#)] [[PubMed](#)]
65. Warth, H.; Mülhaupt, R.; Hoffmann, B.; Lawson, S. Polyester networks based upon epoxidized and maleinated natural oils. *Die Angew. Makromol. Chem.* **1997**, *249*, 79–92. [[CrossRef](#)]

66. Zhang, W.; Liu, W.; Li, H.; Hubbe, M.A.; Yu, D.; Li, G.; Wang, H. Improving stability and sizing performance of alkenylsuccinic anhydride (ASA) emulsion by using melamine-modified laponite particles as emulsion stabilizer. *Ind. Eng. Chem. Res.* **2014**, *53*, 12330–12338. [[CrossRef](#)]
67. Calisi, N.; Giuliani, A.; Alderighi, M.; Schnorr, J.M.; Swager, T.M.; Di Francesco, F.; Pucci, A. Factors affecting the dispersion of MWCNTs in electrically conducting SEBS nanocomposites. *Eur. Polym. J.* **2013**, *49*, 1471–1478. [[CrossRef](#)]
68. Biver, T.; Criscitiello, F.; Di Francesco, F.; Minichino, M.; Swager, T.; Pucci, A. MWCNT/perylene bisimide water dispersions for miniaturized temperature sensors. *Rsc Adv.* **2015**, *5*, 65023–65029. [[CrossRef](#)]
69. Criscitiello, F.; Scigliano, A.; Bianco, R.; Beccia, M.R.; Biver, T.; Pucci, A. Perylene bisimide metal complexes as new MWCNTs dispersants: Role of the metal ion in stability and temperature sensing. *Colloids Surf. A Physicochem. Eng. Asp.* **2017**, *516*, 32–38. [[CrossRef](#)]
70. Di Sacco, F.; Pucci, A.; Raffa, P. Versatile multi-functional block copolymers made by atom transfer radical polymerization and post-synthetic modification: Switching from volatile organic compound sensors to polymeric surfactants for water rheology control via hydrolysis. *Nanomaterials* **2019**, *9*, 458. [[CrossRef](#)]
71. den Hoed, F.; Pucci, A.; Picchioni, F.; Raffa, P. Design of a pH-responsive conductive nanocomposite based on MWCNTs stabilized in water by amphiphilic block copolymers. *Nanomaterials* **2019**, *9*, 410. [[CrossRef](#)] [[PubMed](#)]
72. Araya-Hermosilla, A.E.; Carlotti, M.; Picchioni, F.; Mattoli, V.; Pucci, A. Electrically-conductive polyketone nanocomposites based on reduced graphene oxide. *Polymers* **2020**, *12*, 923. [[CrossRef](#)] [[PubMed](#)]
73. Matzeu, G.; Pucci, A.; Savi, S.; Romanelli, M.; Di Francesco, F. A temperature sensor based on a MWCNT/SEBS nanocomposite. *Sens. Actuators A Phys.* **2012**, *178*, 94–99. [[CrossRef](#)]
74. Giuliani, A.; Placidi, M.; Di Francesco, F.; Pucci, A. A new polystyrene-based ionomer/MWCNT nanocomposite for wearable skin temperature sensors. *React. Funct. Polym.* **2014**, *76*, 57–62. [[CrossRef](#)]
75. Paoletti, C.; He, M.; Salvo, P.; Melai, B.; Calisi, N.; Mannini, M.; Cortigiani, B.; Bellagambi, F.G.; Swager, T.M.; Di Francesco, F.; et al. Room temperature amine sensors enabled by sidewall functionalization of single-walled carbon nanotubes. *RSC Adv.* **2018**, *8*, 5578–5585. [[CrossRef](#)] [[PubMed](#)]
76. Lee, J.H.; Shin, D.W.; Makotchenko, V.G.; Nazarov, A.S.; Fedorov, V.E.; Yoo, J.H.; Yu, S.M.; Choi, J.-Y.; Kim, J.M.; Yoo, J.-B. The superior dispersion of easily soluble graphite. *Small* **2010**, *6*, 58–62. [[CrossRef](#)]
77. Wang, S.; Zhang, Y.; Abidi, N.; Cabrales, L. Wettability and surface free energy of graphene films. *Langmuir* **2009**, *25*, 11078–11081. [[CrossRef](#)]
78. Konios, D.; Stylianakis, M.M.; Stratakis, E.; Kymakis, E. Dispersion behaviour of graphene oxide and reduced graphene oxide. *J. Colloid Interface Sci.* **2014**, *430*, 108–112. [[CrossRef](#)]
79. Wu, J.-B.; Lin, M.-L.; Cong, X.; Liu, H.-N.; Tan, P.-H. Raman spectroscopy of graphene-based materials and its applications in related devices. *Chem. Soc. Rev.* **2018**, *47*, 1822–1873. [[CrossRef](#)]
80. Vryonis, O.; Andritsch, T.; Vaughan, A.S.; Lewin, P.L. An alternative synthesis route to graphene oxide: Influence of surface chemistry on charge transport in epoxy-based composites. *J. Mater. Sci.* **2019**, *54*, 8302–8318. [[CrossRef](#)]
81. Cançado, L.G.; Jorio, A.; Ferreira, E.H.M.; Stavale, F.; Achete, C.A.; Capaz, R.B.; Moutinho, M.V.O.; Lombardo, A.; Kulmala, T.S.; Ferrari, A.C. Quantifying defects in graphene via raman spectroscopy at different excitation energies. *Nano Lett.* **2011**, *11*, 3190–3196. [[CrossRef](#)] [[PubMed](#)]
82. Muhammad Hafiz, S.; Ritikos, R.; Whitcher, T.J.; Razib, N.M.; Bien, D.C.S.; Chanlek, N.; Nakajima, H.; Saisopa, T.; Songsiriritthigul, P.; Huang, N.M.; et al. A practical carbon dioxide gas sensor using room-temperature hydrogen plasma reduced graphene oxide. *Sens. Actuators B Chem.* **2014**, *193*, 692–700. [[CrossRef](#)]
83. Qi, X.; Pu, K.-Y.; Zhou, X.; Li, H.; Liu, B.; Boey, F.; Huang, W.; Zhang, H. Conjugated-polyelectrolyte-functionalized reduced graphene oxide with excellent solubility and stability in polar solvents. *Small* **2010**, *6*, 663–669. [[CrossRef](#)] [[PubMed](#)]
84. Yang, D.; Velamakanni, A.; Bozoklu, G.; Park, S.; Stoller, M.; Piner, R.D.; Stankovich, S.; Jung, I.; Field, D.A.; Ventrice, C.A.; et al. Chemical analysis of graphene oxide films after heat and chemical treatments by X-ray photoelectron and Micro-Raman spectroscopy. *Carbon* **2009**, *47*, 145–152. [[CrossRef](#)]
85. Santra, S.; Hu, G.; Howe, R.C.T.; De Luca, A.; Ali, S.Z.; Udrea, F.; Gardner, J.W.; Ray, S.K.; Guha, P.K.; Hasan, T. CMOS integration of inkjet-printed graphene for humidity sensing. *Sci. Rep.* **2015**, *5*, 17374. [[CrossRef](#)] [[PubMed](#)]

86. Nettleton, D. Chapter 6—Selection of variables and factor derivation. In *Commercial Data Mining*; Nettleton, D., Ed.; Morgan Kaufmann: Boston, MA, USA, 2014; pp. 79–104. [\[CrossRef\]](#)
87. Midya, A.; Mukherjee, S.; Roy, S.; Santra, S.; Manna, N.; Ray, S.K. Selective chloroform sensor using thiol functionalized reduced graphene oxide at room temperature. *Mater. Res. Express* **2018**, *5*, 025604. [\[CrossRef\]](#)
88. Ponnamm, D.; Goutham, S.; Sadasivuni, K.K.; Rao, K.V.; Cabibihan, J.J.; Al-Maadeed, M.A.A. Controlling the sensing performance of rGO filled PVDF nanocomposite with the addition of secondary nanofillers. *Synth. Met.* **2018**, *243*, 34–43. [\[CrossRef\]](#)
89. Some, S.; Xu, Y.; Kim, Y.; Yoon, Y.; Qin, H.; Kulkarni, A.; Kim, T.; Lee, H. Highly sensitive and selective gas sensor using hydrophilic and hydrophobic graphenes. *Sci. Rep.* **2013**, *3*, 1868. [\[CrossRef\]](#)
90. Currie, L.A. Nomenclature in evaluation of analytical methods including detection and quantification capabilities (IUPAC Recommendations 1995). *Pure Appl. Chem.* **1995**, *67*, 1699–1723. [\[CrossRef\]](#)



© 2020 by the authors. Licensee MDPI, Basel, Switzerland. This article is an open access article distributed under the terms and conditions of the Creative Commons Attribution (CC BY) license (<http://creativecommons.org/licenses/by/4.0/>).